



## Rejecting incomplete charge-collection events in CdZnTe and other semiconductor detectors

A.E. Bolotnikov\*, G.S. Camarda, Y. Cui, G. De Geronimo, J. Fried, R. Gul, A. Hossain, K. Kim, G. Yang, E. Vernon, R.B. James

Brookhaven National Laboratory, Upton, NY, USA

### ARTICLE INFO

#### Article history:

Received 10 August 2011

Received in revised form

4 October 2011

Accepted 14 October 2011

Available online 9 November 2011

#### Keywords:

CdZnTe detectors

Virtual Frisch-grid detectors

Crystal defects

Event recognition

### ABSTRACT

In an ideal single-carrier-type gamma ray detector, the amplitudes of the signals and the carrier drift times are correlated variables. However, if the charges produced by an incident photon are not fully collected, as is the case in CdZnTe detectors containing crystal defects, the above correlation does not hold. This permits the application of an event recognition algorithm to identify these incomplete charge collection (ICC) events, caused by the “bad” regions inside a detector, so that they can be removed from pulse height spectra. The ICC events primarily contribute to the Compton continuum and the low-energy tail of the photopeak. Thus, rejecting such events should not affect significantly the photopeak efficiency, but should improve the spectral response, e.g., the peak-to-Compton ratio, for a detector fabricated from material with relaxed crystal quality requirements. Such crystals are those currently available from vendors. The use of stronger ICC correlation-function rejection criteria can improve the energy resolution of these lower-quality crystals, but at the price of a loss in photoefficiency.

Published by Elsevier B.V.

### 1. Introduction

Innovative ASIC-based readout electronics able to provide the amplitudes of charge signals and the drift times of carriers were recently developed for room-temperature semiconductor gamma-ray detectors. This opened opportunities for using new data-reduction techniques that significantly improve the detector's performances and expand their capabilities [1,2]. An example of such techniques is the Compton events reconstruction algorithm developed for pixel detectors [3–5]. In this paper, we describe an algorithm proposed for rejecting incomplete charge collection (ICC) events in CdZnTe (CZT) detectors whose performances are strongly affected by the crystal defects. The rejecting the ICC events will allow the developers to use the average-grade CZT crystals with high contents of the extended defects.

The amount of charge loss by the electron cloud in CZT detectors depends on the types of the defects. Some, such as Te inclusions, cause small charge losses, which cumulatively could result in significant fluctuation of the total collected charge and degrade the energy resolution. Others, such as subgrain boundaries, trap significant amounts of the charge produced by an incident photon; in pulse-height spectra such ICC events are

moved from a photopeak area to a Compton continuum, thereby lowering the device's photopeak efficiency without changing its energy resolution. Furthermore, since ICC events primarily contribute to the Compton continuum and the low-energy tail of the photopeak, rejecting them would not affect the photopeak detection efficiency. This can considerably improve the performance (sensitivity) of detectors fabricated from the crystals with relaxed requirements on material quality. Such crystals typically are those now available from vendors. The use of stronger constraints on the correlation function of the rejecting algorithm can also help to improve the energy resolution. However, this will lower the photopeak efficiency of a device.

The algorithm was originally developed for virtual Frisch-grid CZT detectors; nevertheless, it can be employed for practically any single-type charge-carrier detector in which the amplitudes of the cathode- and anode-signals and the electrons' drift times are measured independently. For example, with modifications, this technique is suitable for strip and pixel detectors. Its usage is extendable to rejecting events that resemble the charge loss caused by crystal defects, e.g., events interacting very close to the collecting electrodes or near the detectors' edges. In pixel detectors, charge sharing among several anodes due to diffusion or multiple interaction points mimics ICC events. In such cases, the cathode still collects the full charge, while individual anodes collect the fractions of the total charge resembling the ICC event. The high-probability multiple interaction-point events in

\* Corresponding author. Tel.: +1 631 344 8014; fax: +1 631 344 3374.  
E-mail address: [bolotnik@bnl.gov](mailto:bolotnik@bnl.gov) (A.E. Bolotnikov).

large-volume detectors can lower the quality of the rejection algorithm by broadening the correlation curve. Accordingly, one must consider the trade-off between the loss of efficiency and the actual spectral improvements.

## 2. Description of the algorithm

Regardless of the type of single-type charge-carrier device, viz., co-planar, [6,7], pixel [8,9] or virtual Frisch-grid [10–12] detector, the dependencies of the amplitudes of the anode and cathode signals on the locations of the interaction points exhibit a common behavior [13]. To the first order, they are approximated by the two linear functions, as illustrated in Fig. 1 for a generalized device with a single anode and cathode. The amplitude of the signal generated on the anode by a point-like unit charge is practically independent of the location of the interaction points, except for the narrow region between the anode and virtual Frisch-grid [14,15], while the amplitude of the cathode swings between 0 and 1. The slopes of both dependences in the cathode-to-grid region reflect the inefficiency of shielding by the virtual grid. Such diverse behaviors of the signals from the cathode and anode allow us to use the cathode-to-anode ratio,  $C/A$ , versus the electron cloud's drift time,  $T$ , as a unique function of the device correlating the cathode- and anode-amplitudes and drift times

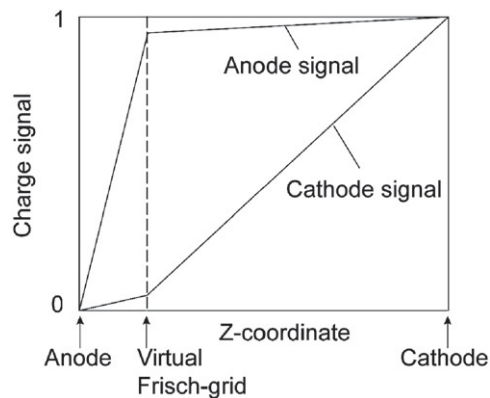


Fig. 1. Typical dependencies of the output signals of the cathode and anode output signals versus drift distance in a single-type charge-carrier device.

measured for every detected event:

$$R(T) = \frac{C}{A}. \quad (1)$$

Every device (or pixel) has its unique correlation function. Sometimes, as we found, it is more convenient to use the product of the cathode-to-anode ratio and the drift time,  $(C/A)T$ .

In the  $R$ - $T$  coordinate space, a single dot represents each interaction event. In the ideal detector, the dots should lay on the line described by the correlation function  $R$ . In practical detectors, most dots (events) still follow the curve within a narrow band determined by the electronic noise, except for the ICC events that fall outside the band. This different behavior distinguishes between the normal events and ICC events caused by the crystal defects or by other processes, e.g., charge sharing in devices with multiple anodes, or edge effects. By choosing a certain acceptance corridor around the curve, one can control the fraction of the rejected versus accepted events. The dots corresponding to multiple interaction-point events may also fall outside the band, causing a loss in photopeak efficiency. However, in vertical virtual Frisch-grid detectors and pixel detectors, multiple interaction-points events corresponding to the same readout voxel are rare. Fig. 2 shows Monte-Carlo simulated distributions of the cathode (a), anode (b) and the ratio  $C/A$  versus drift time (c) for a  $6 \times 6 \times 15 \text{ mm}^3$  virtual Frisch-grid detector. All the distributions in Fig. 2 were normalized to a maximum channel of 662. In the simulation, we used an exact weighting potential to calculate dependences of the signals from the cathode and anode versus the drift time in a defect-free ideal detector. The device was flood-illuminated from the cathode side with 662-keV gamma rays. The combined electronic- and statistical-noise was assumed to be 0.5% at 662 keV. For multiple interaction-points events, we measured the drift time at the arrival time of the last electron cloud. The low-energy threshold was set to 25 keV. Our simulations predict that  $\sim 25\%$  of the events fall outside the 20-channel wide corridor around a curve representing the correlation function evaluated for the single interaction point events. Increasing the acceptance corridor to 40 channels (shown in Fig. 2(c)) reduces the number of wrongly rejected events down to 15%. In pixel detectors with small pixel sizes, the fraction of incorrectly rejected events is expected to be significantly smaller. In comparison, in a large area device, e.g., a  $20 \times 20 \times 15 \text{ mm}^3$  co-planar grid detector,  $\sim 40\%$  of the total number of the events (photopeak and Compton continuum) and  $\sim 60\%$  of the photopeak events will be misidentified

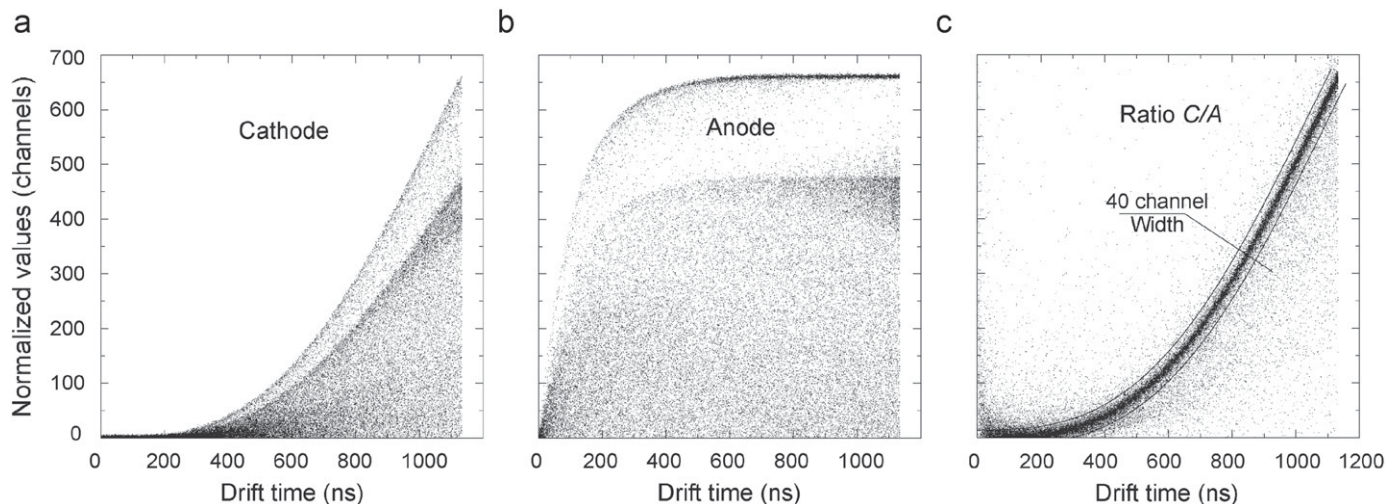


Fig. 2. Distributions of the normalized (a) cathode signals, (b) anode signals, and (c) the cathode-to-anode ratio  $C/A$  versus the drift time,  $T$ , simulated for a defect-free ideal  $6 \times 6 \times 15 \text{ mm}^3$  virtual Frisch-grid detector. The detector was flood-illuminated from the cathode side by 662-keV gamma rays.

rejected. The algorithm will be less beneficial in such cases. A trade-off must be considered between the loss of photoefficiency and the actual spectral improvements achieved, which would depend on the photon energy and crystal quality.

### 3. Test results

To illustrate applicability of the algorithm we investigated performance of two  $6 \times 6 \times 15 \text{ mm}^3$  virtual Frisch-grid detectors (with low and high contents of the extended defects) developed in our laboratory [12] and a  $20 \times 20 \times 15 \text{ mm}^3$  prototype of the pixilated (3D) detector developed by He et al. [9].

#### 3.1. Virtual Frisch-grid detectors

The ICC events rejection algorithm was applied to improve the spectral responses of two  $6 \times 6 \times 15 \text{ mm}^3$  virtual Frisch-grid detectors, with relatively low and high contents of the extended defects. The detectors were fabricated from parallelepiped-shaped CZT crystals furnished with two planar contacts deposited on their smaller sides. Ultra-thin polyester shrink tube was used to encapsulate the crystals [12] prior placing a 5-mm wide shielding electrode (a strip cut from the aluminum tape) over a polyester layer near the anode. During the measurements, the detectors were

flood-illuminated with a  $^{137}\text{Cs}$  source located  $\sim 1 \text{ cm}$  above the cathode. The Endicott charge-shaping preamplifiers were used to read out the signals from the anode and the cathode, which then were digitized with a LeCroy Waverunner. The waveforms were processed to evaluate the amplitudes of the signals and the electron drift times for each interaction event [12]. Each waveform contained 1000 sampling points of which the first 100 data points were used to calculate the waveform baselines and the standard deviation of the noise. The event arrival time was approximated first as the sample number at which the signal reaches a level of two standard deviations of noise above the baseline. Then, a narrow region around this sample was selected to carry out the linear backward interpolation of the pulse's leading edge. The intersection of the interpolation line with the baseline yielded the event's arrival time. With this approach, we assessed a time resolution (FWHM) of  $\sim 10 \text{ ns}$ , estimated via the coincidence signals read out from a  $\text{BaF}_2$  scintillator when annihilation photons from a  $^{68}\text{Ge}$  source were used to generate signals in both detectors. Next, the algorithm determines the time of the electron cloud's arrival at the anode, using the fast-rising signal from the anode. We determined this time as the intersection of two lines: One extrapolates forward a pulse's leading edge; the second extrapolates backward the pulse's saturated amplitude. Finally, the signals' amplitudes (anode and cathode) were calculated as the difference between the saturated part of a waveform (a pulse amplitude) and the baseline that we

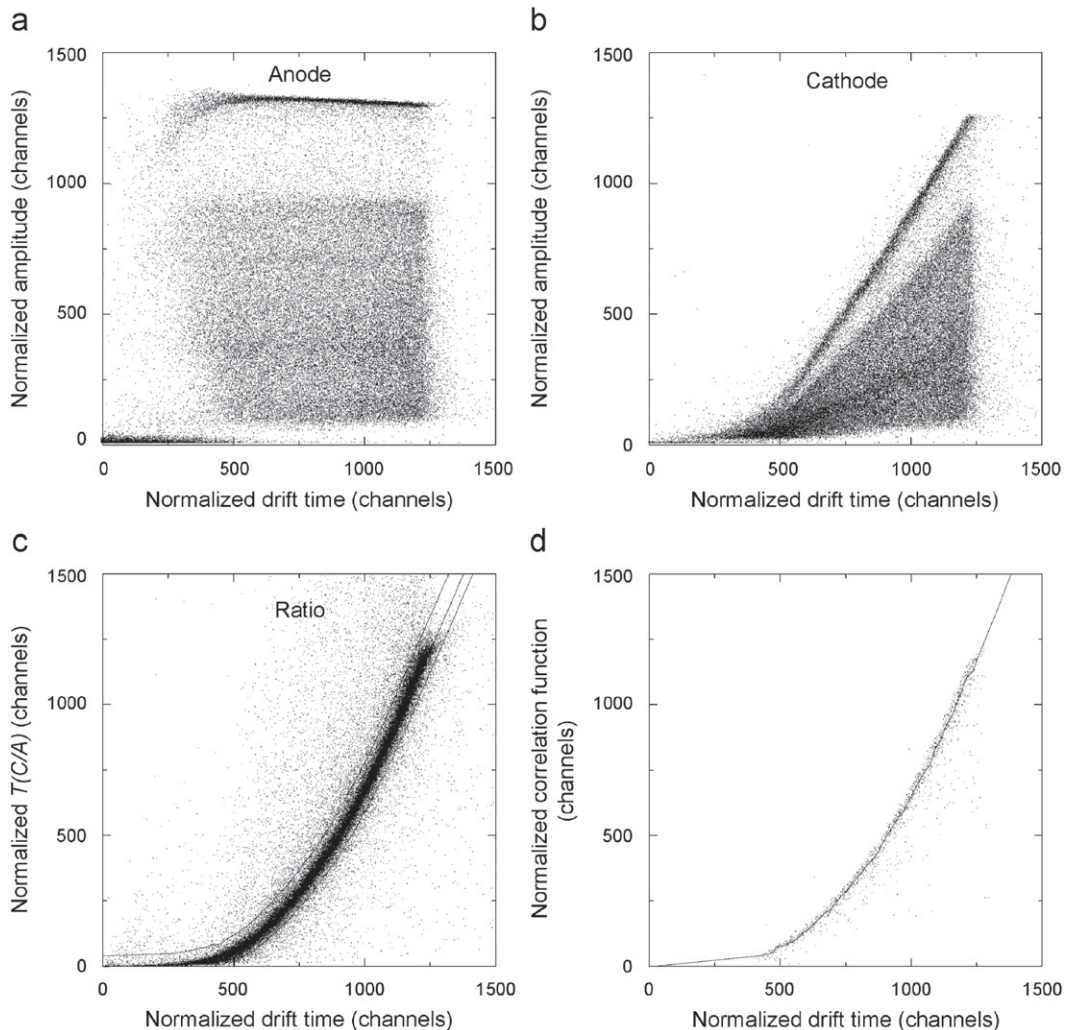


**Fig. 3.** Distributions of the normalized output signals measured from the anode (a), cathode (b), and the product of  $(C/A)T$  (c) versus the normalized drift time  $T$ . The correlation function (d) was obtained by selecting the photoabsorption events that fall under the 662-keV photopeak in the pulse-height spectrum.

obtained by averaging the points within the adjacent time window from the left to the beginning of the pulse (the event's arrival time). The same size window located after the electron cloud's arrival time and delayed by it is used to calculate the pulse level.

Fig. 3(a–c), respectively, show the correlations of the normalized signals read out from the anode,  $A$ , cathode,  $C$ , and the ratio  $C/A$  versus the drift time,  $T$ , measured for the detector with a relatively low content of extended defects. As noted before, each dot in these distributions represents a detected event. Fig. 3(a) and (b) reveal that the dots corresponding to 662-keV photoabsorption events concentrate around the curves representing the dependencies of the anode- and cathode-signals versus the drift time. These dependencies are similar to those depicted in Fig. 2. The broad continuums of the dots attributed to the Compton scattering and ICC events also are evident in Fig. 3(a) and (b). Remarkably, these distributions collapsed into a narrow corridor when we plotted them as the ratio  $C/A$  versus  $T$  (Fig. 3(c)). The two solid lines in Fig. 3(c) define a 100-channel-wide band around the correlation function,  $R(T)$ , which we derived by selecting only the full-energy absorption events that fell under the 662-keV photopeak (Fig. 3(d)). The dots outside the band represent the ICC events mainly originating from charge trapping at the detector's side surfaces; these events must be rejected from the final pulse-height spectra. We note that the slow-decaying slope of the correlation curve in Fig. 3(a) is due to the charge trapping effect that can be corrected electronically.

Fig. 4 depicts the pulse-height spectra before (a) and after (b) rejecting the events outside the acceptance band, thereby resulting in a notable reduction of the continuum, while the

photopeak remains practically unchanged (4% reduction). The initial spectrum was corrected for charge trapping before rejecting ICC events.

Fig. 5 shows the pulse-height spectra before and after the events rejection, evaluated for a virtual Frisch-grid detector with a poor performance attributed to its high content of extended defects. As in the previous case, rejecting the events significantly reduces their numbers in the continuum area, while the counts at the photopeak fall only by  $\sim 6\%$ . As before, the original spectrum was corrected for charge trapping before rejecting ICC events.

To illustrate how the algorithm works for multiple gamma-lines, we carried out measurements with a  $^{133}\text{Ba}$  source. We superposed a  $^{137}\text{Cs}$  source to evaluate the correlation curve we used for rejection. Fig. 6 shows the correlations of the signals read out from the anode and cathode, and the product of  $(C/A)T$  versus  $T$  measured for the detector with a low content of extended defects. As described before, each dot in these distributions represents a detected event. Similar to the distribution in Fig. 3, the concentrations of dots correspond to the multiple gamma-lines emitted by the  $^{133}\text{Ba}$  source. As is evident, the low-amplitude cathode signals generated by low-energy phonons,  $< 100$  keV, interacting new the cathode were not evaluated correctly. These events broaden the distributions of  $(C/A)T$  versus  $T$  (c) and long drift times. Consequently, these events are mistakenly rejected, as is illustrated in Fig. 7 showing the pulse-height spectra before and after rejection. The original spectrum was corrected for charge trapping before rejecting ICC events. Using better calibrated electronics with a lower energy threshold, it would be possible to reduce the number of wrongly rejected low-energy events.

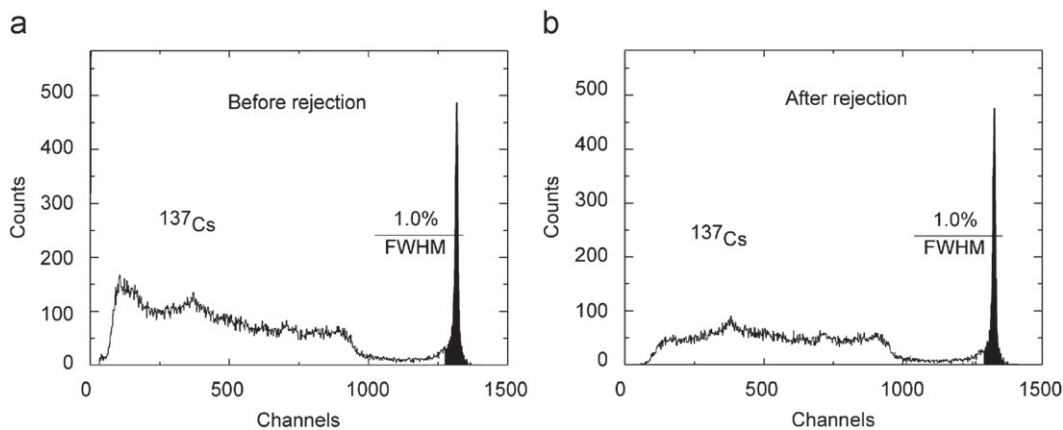


Fig. 4. Pulse-height spectra of  $^{137}\text{Cs}$  before (a) and after (b) applying events rejection for a crystal with a relatively high content of extended defects.

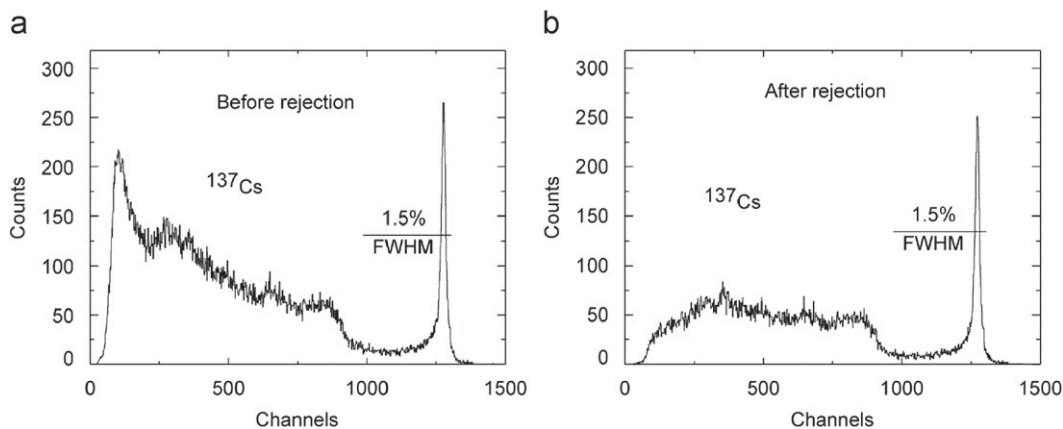
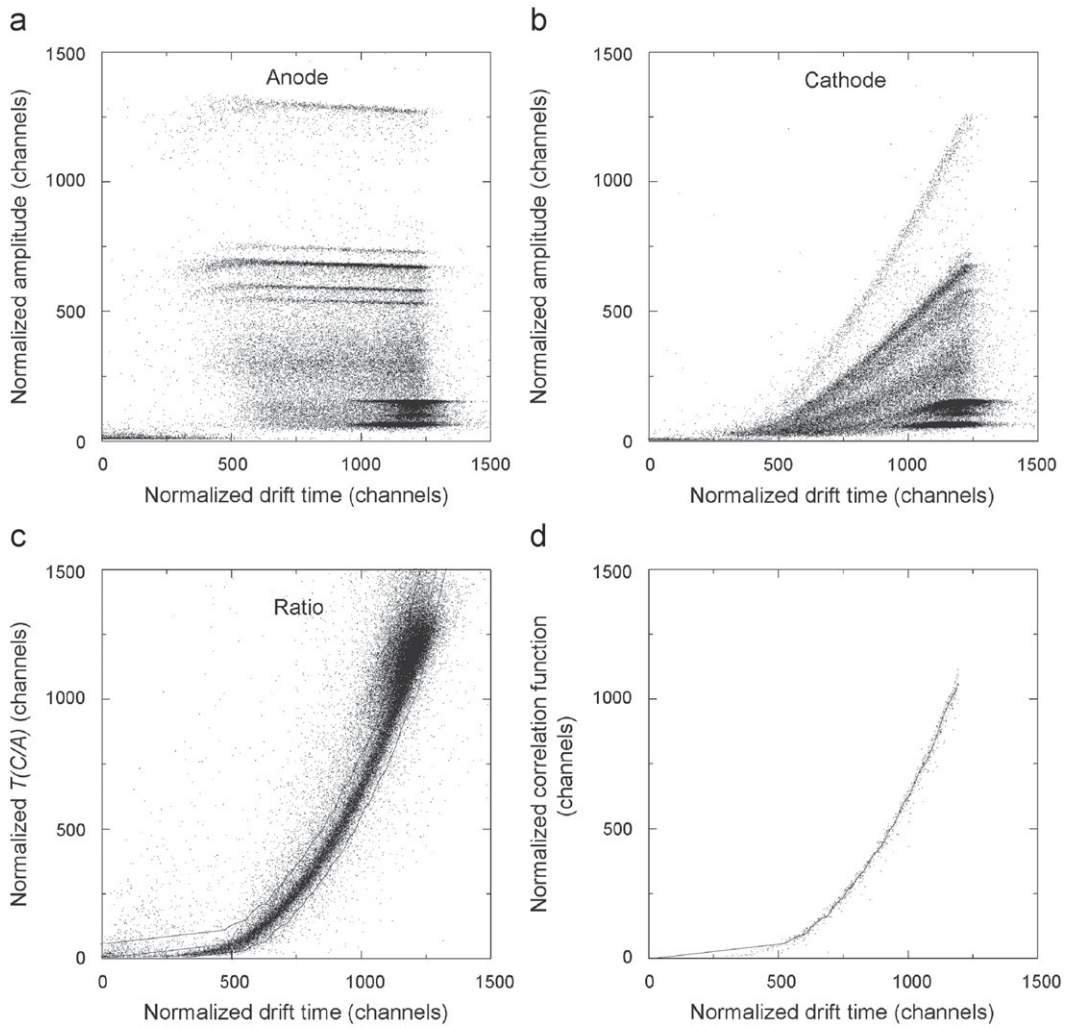
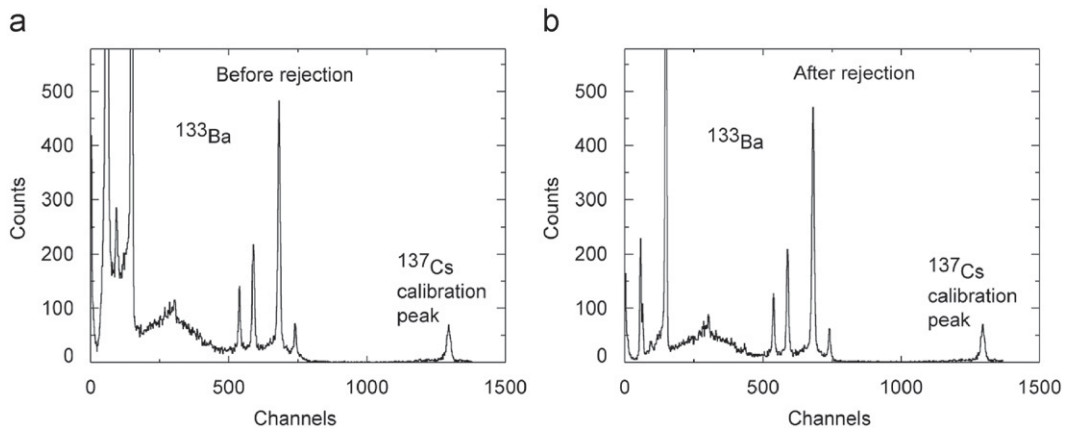


Fig. 5. Pulse-height spectra of  $^{137}\text{Cs}$  before (a) and after (b) applying the events rejection for a crystal with a relatively high content of extended defects.



**Fig. 6.** Distributions of the normalized output signals measured from the anode (a), cathode (b), and the product of  $(C/A)T$  (c) versus the normalized drift time  $T$  measured for a  $^{133}\text{Ba}$  source. The correlation function (d) was obtained by selecting the photoabsorption events from the  $^{137}\text{Cs}$  source.



**Fig. 7.** Pulse-height spectra of  $^{133}\text{Ba}$  before (a) and after (b) applying events rejection for the crystal with a low content of extended defects.

### 3.2. Pixel detectors

In a pixelated device the readout ASIC provides information on the amplitudes and drift times for each of the event's interaction points, so supporting a better handling of multiple interaction points events. In the following example, we employed the same approach used for the virtual Frisch-grid detectors. BNL's

Instrumentation Division made available a data stream generated by readout electronics from a  $20 \times 20 \times 15 \text{ mm}^3$  CZT detector [16]. The detector was flood-illuminated with a  $^{137}\text{Cs}$  source. In this example, we selected events that forced readout of the signals from a particular representative pixel, regardless of which pixel actually was triggered. From these data, we plotted the distribution of  $(A_{\text{Cathode}}/A_{\text{Pixel}})t$  versus  $t$ ; the corresponding pulse-

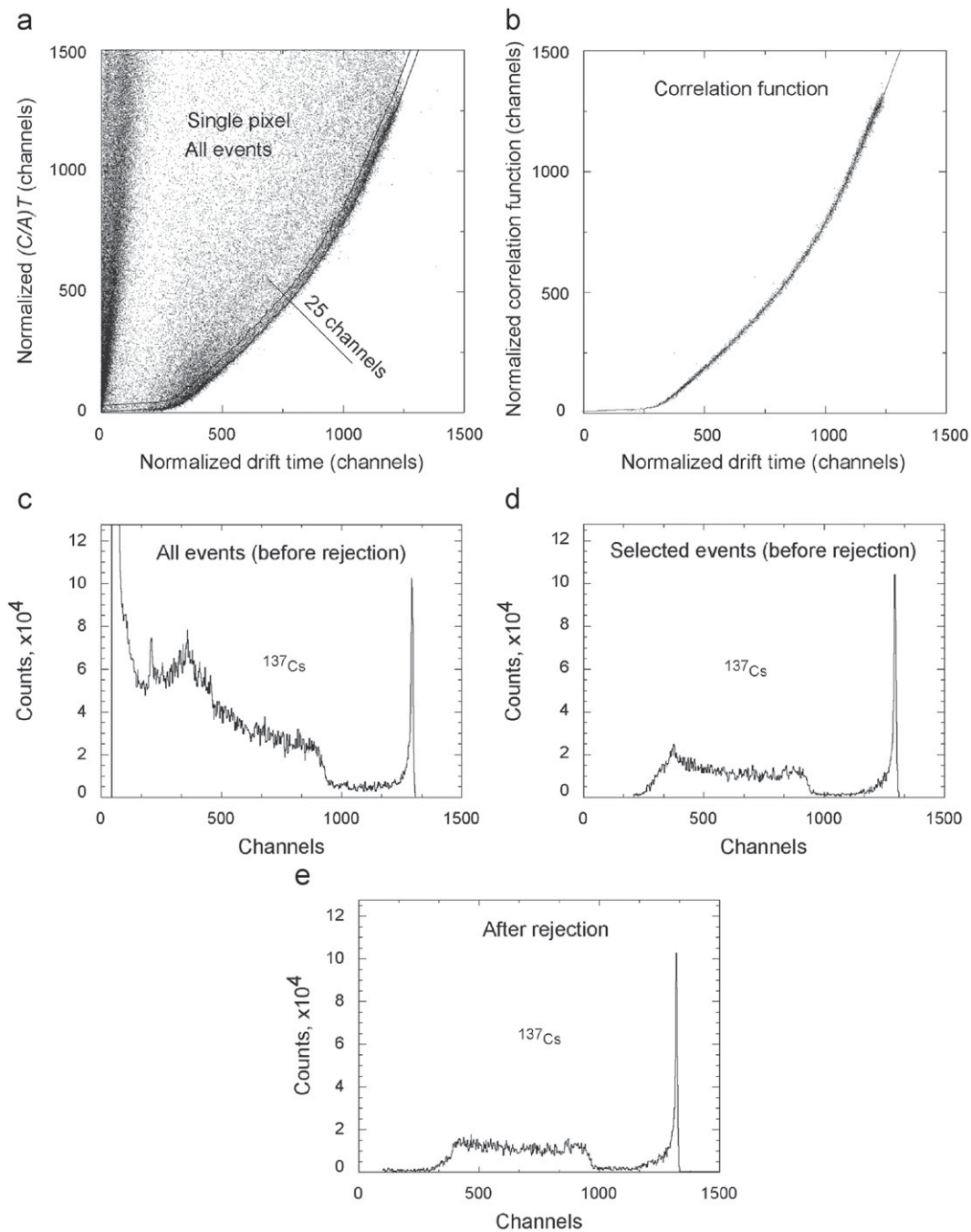


**Fig. 8.** (a) Distribution of  $(C/A)T$  versus  $T$  plotted for all events. (b) Correlation function evaluated by selecting the photoabsorption events. (c) Pulse-height spectrum evaluated for all events. (d) Pulse-height spectrum evaluated for the true single-pixel events. (e) Pulse-height spectrum evaluated for all events after rejection.

height spectra are shown in Fig. 8(a) and (c), respectively. To evaluate the correlation function,  $r$ , we selected the events under the photopeak (i.e., full-energy deposition events) and plotted them in Fig. 8(b), along with a solid line representing the fitting results. We note that the correlation function defines the low edge of the distribution of total events illustrated in Fig. 8(a). By selecting a narrow band (25 channels) around the correlation curve, we identified and rejected the ICC events from the pulse-height spectrum. Fig. 8(e) depicts the “cleaned” spectrum.

By comparing these spectra, we see a significant reduction of the events contributing to the continuum, while the photopeak remains unchanged. Cutting the spectrum around a channel of 300 corresponds to the trigger threshold we used to collect the data. This cut is not apparent in the total events spectrum because

of the charge-sharing effect when adjacent pixels were triggered. Since we rejected all possible kinds of ICC events, including charge sharing and Compton scattering that resemble ICC events, the only ones left in the spectrum in Fig. 8(e) are those that triggered the pixel. For comparison, we show in Fig. 8(d) the pulse-height spectrum of the electronically selected events that triggered the pixel without charge sharing (true single-pixel events). The latter also shows a threshold cut; however, compared with the former, it has a slightly higher level of continuum events in the low-channel regions. We attribute this to some fraction of the “undetected” multiple interaction-points events, since not all of the device’s pixels were operating. We did not expect that this particular selected pixel would detect many of the ICC events caused by crystal defects because of the high-quality material

used to fabricate the detector. We note that FWHMs of the photopeaks in these spectra were less than 0.9%.

For such multiple events, we can use the amplitude and timing information for each interaction point. A fraction of the total cathode signal,  $C_i$ , generated by the charge deposited within the  $i$ th pixel can be estimated with good accuracy by

$$C_i = C \frac{A_i T_i}{\sum_j A_j T_j}. \quad (2)$$

The summing is taken over all the interaction points. In this formula, we assumed that, at least in the first approximation, the signal generated on the cathode by the point-like charge was proportional to the distance to the anode, i.e., the drift time. When  $C_i$  is known, the cathode-to-anode ratios (1), measured *a priori* for every pixel, can be used to reject the ICC events.

#### 4. Conclusions

We demonstrated an algorithm for rejecting incomplete charge-collection (ICC) events caused by extended defects in CdZnTe and potentially other semiconductor detectors (e.g., HgI<sub>2</sub>, CdTe, and TlBr). Excluding the ICC events allows one to use average-grade CZT crystals with a high content of the extended defects. Although the algorithm was developed for virtual Frisch-grid CZT detectors, it can be employed for any single-type charge carrier detector wherein the amplitudes of the cathode- and anode-signals and the electrons' drift times are measured independently. The multiple interaction-point events that have high probabilities of occurrence in large-volume detectors degrade the quality of the rejection algorithm by broadening the correlation curve. In such cases, a trade-off must be considered between the loss of photoefficiency and the actual improvements achieved, which would depend on the photon energy and crystal quality.

#### Acknowledgments

This work was supported by the US Department of Energy, Office of Nonproliferation Research and Development, Grant no.

NA-22, Defense Threat Reduction Agency, and BNL's Technology Maturation Award. The manuscript has been authored by Brookhaven Science Associates, LLC under Contract no. DE-AC02-98CH1-886 with the US Department of Energy. The United States Government retains, and the publisher, by accepting the article for publication, acknowledges, a world-wide license to publish or reproduce the published form of this manuscript, or allow others to do so, for the United States Government purposes.

#### References

- [1] G. De Geronimo, E. Vernon, K. Ackley, J. Fried, P. O'Connor, A. Dragone, Z. He, C. Herman, F. Zhang, IEEE Transactions on Nuclear Science NS-55 (3) (2008) 1593.
- [2] F.A. Harrison, W.R. Cook, H. Miyasaka, R. McLean, Cadmium zinc telluride pixel detectors for hard x-ray astrophysics, in: K. Iniewski (Ed.), Semiconductor Radiation Detection Systems, CRC Press, 2010 (Chapter 3).
- [3] E. Aprile, A. Bolotnikov, D. Chen, R. Mukherjee, Nuclear Instruments & Methods A 327 (1993) 216.
- [4] S.E. Boggs, P. Jean, Astronomy & Astrophysics Supplement Series 145 (2000) 311.
- [5] C.E. Lehner, Z. He, F. Zhang, IEEE Transactions on Nuclear Science NS-51 (2004) 1618.
- [6] V.P. Miroshnichenko, B.U. Rodionov, E. Shuvalova, The Method of Detection of Gamma Radiation, USSR Patent SU-1264723A, Issued June 15, 1986.
- [7] P.N. Luke, Applied Physics Letters 65 (22) (1995) 2884 (also see US Patent 5,530,249 by P.N. Luke, 1996).
- [8] H.H. Barrett, J.D. Eskin, H.B. Barber, Physical Review Letters 75 (1) (1995) 156.
- [9] Z. He, W. Li, G.F. Knoll, D.K. Wehe, J. Berry, C.M. Stahle, Nuclear Instruments & Methods A 422 (1999) 173.
- [10] D.S. McGregor, R.A. Rojeski, High-Resolution Ionization Detector and Array of Such Detectors, US Patent 6175120, Issued January 16, 2001.
- [11] G. Montemont, M. Arques, L. Verger, J. Rustique, IEEE Transactions on Nuclear Science NS-48 (2001) 278.
- [12] J.K. Polack, M. Hirt, J. Sturgess, N.D. Sferrazza, A.E. Bolotnikov, S. Babalola, G.S. Camarda, Y. Cui, S.U. Egarievwe, P.M. Fochuk, R. Gul, A. Hossain, K. Kim, O.V. Kopach, L. Marchini, G. Yang, L. Xu, R.B. James, Nuclear Instruments & Methods A 621 (2010) 424.
- [13] G. Knoll, Radiation Detection and Measurement, 3rd ed., Wiley, New York, 2000.
- [14] O.R. Frisch, Unpublished Report, BR-49, Isotope Analysis of Uranium Samples by Means of their Alpha-Ray Groups, British Atomic Energy Project, 1944.
- [15] O. Buneman, T.E. Cranshaw, J.A. Harvey, Canadian Journal of Research A 27 (1949) 191.
- [16] G. De Geronimo, E. Vernon, K. Ackley, A. Dragone, J. Fried, P.O. Connor, Z. He, C. Herman, F. Zhang, IEEE Transactions on Nuclear Science NS-55 (2008) 1593.